The Astrophysical Journal, 850:170 (10pp), 2017 December 1 https://doi.org/10.3847/1538-4357/aa8ee3

High Dense Gas Fraction in Intensely Star-forming Dusty Galaxies

I. Oteo[1,2], Z-Y. Zhang[1,2], C. Yang[3,4,5,6,7], R. J. Ivison[1,2], A. Omont[6,7], M. Bremer[8], S. Bussmann[1,2], A. Cooray[9], P. Cox[10], H. Dannerbauer[11,12], L. Dunne[1,13], S. Eales[13], C. Furlanetto[14], R. Gavazzi[15], Y. Gao[16], T. R. Greve[17], H. Nayyeri[9], M. Negrello[13], R. Neri[18], D. Riechers[19], R. Tunnard[17], J. Wagg[20], and P. Van der Werf[21]
[1] Institute for Astronomy, University of Edinburgh, Royal Observatory, Blackford Hill, Edinburgh EH9 3HJ, UK; ivanoteogomez@gmail.com
[2] European Southern Observatory, Karl-Schwarzschild-Str. 2, D-85748 Garching, Germany
[3] Purple Mountain Observatory/Key Lab of Radio Astronomy, Chinese Academy of Sciences, Nanjing 210008, PR China
[4] Institut d'Astrophysique Spatiale, CNRS, Univ. Paris-Sud, Université Paris-Saclay, Bât. 121, F-91405 Orsay cedex, France
[5] Graduate University of the Chinese Academy of Sciences, 19A Yuquan Road, Shijingshan District, 10049, Beijing, PR China
[6] CNRS, UMR 7095, Institut d'Astrophysique de Paris, F-75014, Paris, France
[7] UPMC Univ. Paris 06, UMR 7095, Institut d'Astrophysique de Paris, F-75014, Paris, France
[8] H. H. Wills Physics Laboratory, University of Bristol, Tyndall Avenue, Bristol BS8 1TL, UK
[9] Department of Physics and Astronomy, University of California, Irvine, CA 92697, USA
[10] Joint ALMA Observatory—ESO, Av. Alonso de Cordova, 3104, Santiago, Chile
[11] Universidad de La Laguna, Dpto. Astrofísica, E-38206 La Laguna, Tenerife, Spain
[12] Instituto de Astrofísica de Canarias, E-38205 La Laguna, Tenerife, Spain
[13] School of Physics and Astronomy, Cardiff University, The Parade, Cardiff CF24 3AA, UK
[14] School of Physics and Astronomy, Nottingham University, University Park, Nottingham, NG7 2RD, UK
[15] Institut d'Astrophysique de Paris, UMR7095 CNRS-Université Pierre et Marie Curie, 98bis bd Arago, F-75014 Paris, France
[16] Purple Mountain Observatory, Key Lab of Radio Astronomy, 2 West Beijing Road, 210008 Nanjing, PR China
[17] Department of Physics and Astronomy, University College London, Gower Street, London WC1E 6BT, UK
[18] IRAM, 300 rue de la piscine, F-38406 Saint-Martin d'Heres, France
[19] Department of Astronomy, Space Science Building, Cornell University, Ithaca, NY 14853-6801, USA
[20] SKA Organization, Lower Withington Macclesfield, Cheshire SK11 9DL, UK
[21] Leiden Observatory, Leiden University, P.O. Box 9513, NL-2300 RA Leiden, The Netherlands
Received 2017 January 20; revised 2017 August 13; accepted 2017 September 12; published 2017 November 28

Abstract

We present ALMA $J = 3$–2 and VLA $J = 1$–0 observations of the dense molecular gas tracers HCN, HCO^+, and HNC in two lensed, high-redshift starbursts selected from the *Herschel*-ATLAS survey: *H*-ATLAS J090740.0 −004200 (SDP.9, $z_{spec} = 1.575$) and *H*-ATLAS J091043.1−000321 (SDP.11, $z_{spec} = 1.786$). In SDP.9 we have detected all $J = 3$–2 transitions and also HCN(1–0) and HCO^+(1–0). In SDP.11 we have detected HCN(3–2) and HCO^+(3–2). The amplification factors for both galaxies have been determined from subarcsecond-resolution CO and dust emission observations carried out with NOEMA and the SMA. The HNC(1–0)/HCN(1–0) line ratio in SDP.9 suggests the presence of photon-dominated regions, as happens in most local (U)LIRGs. The CO, HCN, and HCO^+ spectral line energy distribution (SLEDs) of SDP.9 are compatible to those found for many local, IR-bright galaxies, indicating that the molecular gas in local and high-redshift dusty starbursts can have similar excitation conditions. We obtain that the correlation between total IR (L_{IR}) and dense line (L_{dense}) luminosity in SDP.9 and SDP.11 and local star-forming galaxies can be represented by a single relation. We argue that the scatter of the L_{IR}–L_{dense} correlation, together with the lack of sensitive dense molecular gas tracer observations for a homogeneous sample of high-redshift galaxies, prevents us from distinguishing differential trends with redshift. Our results suggest that the intense star formation found in some high-redshift, dusty, luminous starbursts is associated with more massive dense molecular gas reservoirs and higher dense molecular gas fractions.

Key words: galaxies: high-redshift – galaxies: ISM – galaxies: starburst – galaxies: star formation

1. Introduction

Active star formation in galaxies occurs in dense regions within molecular clouds. Studying the dense interstellar medium is, therefore, of fundamental importance for our understanding of the formation and evolution of star-forming galaxies. The critical densities of rotational transitions are proportional to $\mu^2\,\nu^3_{J+1,J}$, where μ is the dipole moment and $\nu_{J+1,J}$ is the frequency of the rotational level J of the molecule (Shirley 2015). Because the dipole moments of the HCN, HNC, and HCO^+ molecules are almost 30 times higher than those for CO, the HCN, HNC, and HCO^+ transitions trace a gas component whose critical density could be ∼100–500 times denser than the gas traced by CO for the same rotational level.

Because HCN, HCO^+, and HNC can only be excited in very dense regions, they trace the places where star formation takes place. This is why correlations have been found between the HCN and total IR luminosity (Gao & Solomon 2004b; Privon et al. 2015), although the relation between star formation rate (SFR) and dense gas emission can be also affected by several other physical factors (Krips et al. 2008; Imanishi et al. 2007, 2009; Davies et al. 2012; García-Burillo et al. 2012; Chen et al. 2017). Actually, there are places with dense gas but without star formation, and there are also places with star formation but little dense gas. One of the most obvious cases is the Galactic central region, especially the central molecular zone, where the average H_2 density is $>10^4$ cm^{-3} and there is little star formation compared to normal molecular clouds (Kauffmann et al. 2013; Longmore et al. 2013). The same happens in some local galaxies, such as the Antennae galaxies, the nuclear region of NGC 4039, or NGC 1068 (Ueda et al. 2012; García-Burillo et al. 2014). On the other hand,

Papadopoulos et al. (2014) showed that Arp 193 has much less (<10%) dense gas mass than NGC 6240, while they have similar total IR luminosities and are not heavily affected by active galactic nuclei (AGNs).

One of the main challenges of studying the dense molecular gas via HCN, HCO^+, and HNC transitions is that they are typically faint, about an order of magnitude fainter than CO lines in LIRGs and ULIRGs, and up to two orders of magnitude for normal galaxies (Gao & Solomon 2004a, 2004b; Bussmann et al. 2008; Juneau et al. 2009). Therefore, whereas dense molecular gas tracers have been detected in a fairly large number of galaxies in the local universe (Aalto et al. 2002; Gao & Solomon 2004a, 2004b; Papadopoulos 2007; Baan et al. 2008; Bussmann et al. 2008; Graciá-Carpio et al. 2008; Juneau et al. 2009; Liu et al. 2015; Privon et al. 2015), the detection of HCN, HCO^+, and HNC at high redshift has been limited to a handful of extreme sources such as QSOs, where the probability of detection was higher (Gao et al. 2007; Riechers et al. 2011b). One way to overcome the difficulty of detecting dense molecular gas tracers is taking advantage of the amplification provided by gravitational lensing. The combination of intrinsic far-IR (FIR) brightness, lens amplification, and sensitive instrumentation like the Atacama Large Millimeter/submillimeter Array (ALMA) and the Very Large Array (VLA) makes it possible to carry out studies of faint emission lines that otherwise would require very long integration times.

In this work, we present VLA and ALMA detections of three dense molecular gas tracers, HCN, HCO^+, and HNC, in two lensed ULIRGs selected from the *H*-ATLAS (Eales et al. 2010): *H*-ATLAS J090740.0−004200 (hereafter SDP.9, at $z \sim 1.6$) and *H*-ATLAS J091043.1−000321 (hereafter SDP.11, at $z \sim 1.8$); see Negrello et al. (2010, 2014). The properties of the targets can be found in Table 1, including redshifts, coordinates, intrinsic total IR luminosity, SFR, and dust temperature. All these values have been taken from Bussmann et al. (2013). The amplification factors have been obtained from CO and dust emission observations at subarcsecond spatial resolution carried out with NOEMA and the SMA. The structure of the paper is as follows: Section 2 presents the data used in this work. Section 3 explains the lens modeling of the studied sources. Next, Section 4 presents the molecular line detections and the study of the physical conditions of the gas in our galaxies. Finally, Section 5 summarizes the main conclusions of this work. Throughout this paper we assume a flat universe with $(\Omega_m, \Omega_\Lambda, h_0) = (0.3, 0.7, 0.7)$.

Table 1
Observed Properties of SDP.9 and SDP.11
(Not Corrected from Lens Magnification)

Parameter	SDP.9	SDP.11
R.A.	09:07:40.0	09:10:43.1
Decl.	−00:41:59.8	−00:03:22.8
$T_{\rm dust}$ (K)[a]	43 ± 2	41 ± 1
$L_{\rm IR}$ [$\times 10^{13}\,L_\odot$][a]	6.4 ± 0.1	6.6 ± 0.1
SFR ($M_\odot$ yr^{-1})[a]	∼11,500	∼11,800
$z_{\rm spec}$[b]	1.575 ± 0.005	1.786 ± 0.005
$\mu_{\rm CO}$	5.8 ± 2.9	5.5 ± 1.0
$\mu_{\rm dust}$	4.5 ± 1.9	6.1 ± 1.2
$\mu_{\rm stars}$[c]	6.3 ± 0.3	4.9 ± 0.9
Emission-line Fluxes		
^{12}CO J = 1–0 $I_{\rm CO}$ (Jy km s^{-1})	1.0 ± 0.2	⋯
^{12}CO J = 2–1 $I_{\rm CO}$ (Jy km s^{-1})[d]	6.1 ± 1.2	⋯
^{12}CO J = 3–2 $I_{\rm CO}$ (Jy km s^{-1})	10.1 ± 0.6	⋯
^{12}CO J = 4–3 $I_{\rm CO}$ (Jy km s^{-1})	⋯	8.9 ± 1.0
^{12}CO J = 5–4 $I_{\rm CO}$ (Jy km s^{-1})[b]	25 ± 5	23 ± 8
^{12}CO J = 6–5 $I_{\rm CO}$ (Jy km s^{-1})[b]	33 ± 7	29 ± 10
^{12}CO J = 7–6 $I_{\rm CO}$ (Jy km s^{-1})[b]	⋯	18 ± 14
HCN(1–0) (Jy km s^{-1})	0.17 ± 0.01	<0.19
HCO^+(1–0) (Jy km s^{-1})	0.17 ± 0.01	<0.19
HNC(1–0) (Jy km s^{-1})	<0.08	<0.19
HCN(3–2) (Jy km s^{-1})	0.66 ± 0.11	0.54 ± 0.08
HCO^+(3–2) (Jy km s^{-1})	0.36 ± 0.14	0.36 ± 0.03
HNC(3–2) (Jy km s^{-1})	0.42 ± 0.10	<0.10

Notes.
[a] From Bussmann et al. (2013).
[b] From Lupu et al. (2012).
[c] From Dye et al. (2014).
[d] From Iono et al. (2012).
[e] From Lupu et al. (2012).

2. Data Sets

ALMA observations: SDP.9 and SDP.11 were observed with ALMA in the 3 mm band in compact configuration (project 2012.1.00915.S; PI: R. Lupu) with the aim of detecting their HCN(3–2), HCO^+(3–2), and HNC(3–2) emission lines. For each source, the spectral setup of the observations was defined to sample the three lines simultaneously. The data for each galaxy were reduced independently using standard techniques in CASA. Imaging was done using natural weighting to improve the signal-to-noise ratio (S/N) of the detections. The rms of the cubes is ∼0.14 mJy beam^{-1} in 100 km s^{-1} wide channels, with a synthesized beam of $3\farcs7 \times 2\farcs3$.

VLA observations: The HCN(1–0), HCO^+(1–0), and HNC (1–0) transitions in SDP.9 and SDP.11 have been observed with the National Radio Astronomy Observatory (NRAO) VLA in two different projects: 15B-266 (PI. Thomas Greve) and 14B-259 (PI: C. Yang). In both projects, and for both sources, the spectral setups were defined to cover all three lines simultaneously. The data were manually calibrated by following the standard procedures, including manual flagging and recalibration. In part of the SDP.9 observations, the gain calibrator was J0909 + 0200, which has a weak emission of ∼0.3 Jy; we combined all 24 spectral windows (spws) together in the gain calibration to get enough S/N, instead of calibrating gain solutions spw by spw. By doing this, we assume that the responses of different spws do not vary with frequency. After imaging, carried out with natural weighting to improve the S/N of the detections, the rms reached is ∼0.14 mJy beam^{-1} in 75 km s^{-1} wide channels for SDP.9 and ∼0.22 mJy beam^{-1} in 75 km s^{-1} wide channels for SDP.11. In both observations the synthesized beams are $\sim 3\farcs4 \times 2\farcs3$.

The rest-frame ∼18 GHz emission of SDP.9 and SDP.11 was also observed with the VLA in its most extended configuration at ∼7 GHz (project 12B-189; PI: R. Ivison). Additionally, the ^{12}CO(1–0) transition in SDP.9 was also observed with the VLA in C configuration (project 12A-201; PI: R. Ivison). Both data sets were calibrated in AIPS following the standard prescriptions, including manual flagging of the RFI emission in C band. Imaging was carried out using natural weighting to improve sensitivity. In the 7 GHz continuum maps, the rms and the beam size are similar for both sources:

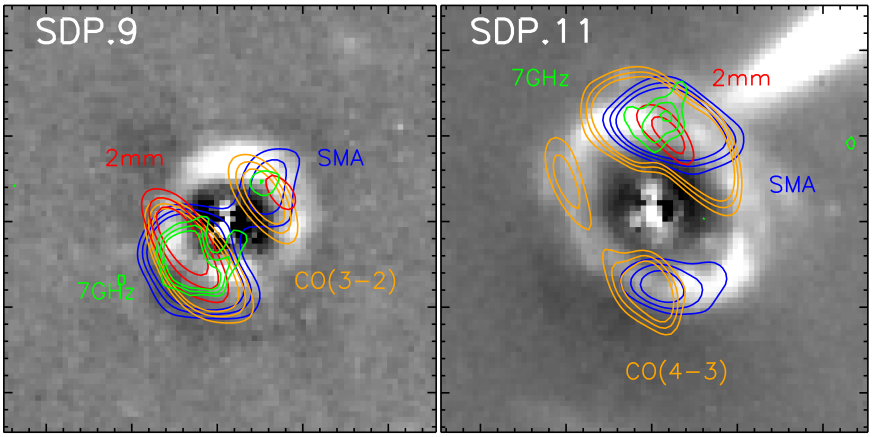

Figure 1. Resolved stellar, dust, molecular gas, and radio continuum emission in the two lensed ULIRGs studied in this work: SDP.9 at $z \sim 1.6$ (left) and SDP.11 at $z \sim 1.8$ (right). The background images represent the stellar emission observed by *HST* (the foreground lenses have been subtracted by fitting their light profiles with GALFIT). The size of each image is $5'' \times 5''$; north is up, east is left. Contours represent the dust (at 870 μm [blue] from the SMA and 2 mm [red] from PdBI), molecular gas (via the CO(3–2) transition; orange), and radio continuum emission (from VLA at 7 GHz; green). All contours are represented from 3σ to 5σ in steps of 1σ. The dense molecular gas and ^{12}CO(1–0) transitions are not shown because they are unresolved owing to the relatively large beam of the ALMA and VLA observations.

$\sim$12 μJy beam^{-1} and $\sim 0\farcs42 \times 0\farcs32$, respectively. The ^{12}CO(1–0) cube for SDP.9 has an rms $\sim$ 0.42 mJy beam^{-1} in 75 km s^{-1} wide channels and a beam size of $\sim 1\farcs6 \times 1\farcs4$. Note that there are no available observations of ^{12}CO(1–0) for SDP.11.

PdBI observations: The ^{12}CO(3–2) emission in SDP.9 and SDP.11 was carried out by the PdBI in its most extended configuration during 2011 January and February (programs UAAA and UBAA; PIs: P. Cox and R. Ivison). The data were calibrated by using the standard techniques with GILDAS. Imaging was carried out using natural weighting to maximize sensitivity. In SDP.9 we reached an rms $\sim$ 0.8 mJy beam^{-1} in 50 km s^{-1} wide channels, while the noise level in SDP.11 is rms $\sim$ 1.2 mJy beam^{-1} in 50 km s^{-1} wide channels. The median beam size of the spectral cubes is $1\farcs10 \times 0\farcs46$ and $0\farcs86 \times 0\farcs36$ for SDP.9 and SDP.11, respectively.

All previous data sets are also combined with available dust continuum observations taken with the SMA (Bussmann et al. 2013) and stellar emission observed with the *Hubble Space Telescope* (*HST*) at near-IR wavelengths (Negrello et al. 2014). We refer the reader to those works for details on the data calibration and reduction. We point out that the overall astrometric uncertainty of the interferometric observations at subarcsecond resolution used in this work is estimated to be lower than $0\farcs2$. Therefore, the comparison between the different morphologies of gas, dust, and stars (see Section 4.1) is not strongly affected by the astrometric uncertainties. Also, we estimate that the absolute flux calibration of all these data sets has an uncertainty of $\sim$15%.

3. Lens Modeling

We have modeled the lensed dust continuum (observed with the SMA at 880 μm) and ^{12}CO(3–2) (observed with the PdBI) emission in SDP.9 and SDP.11 (see Figure 1) by using `uvmcmcfit` (Bussmann et al. 2015), a code designed to model, in the *uv* plane, the emission of gravitationally lensed galaxies observed with interferometers. Note that we have not modeled the PdBI-observed 2 mm continuum owing to the poor S/N. We have not modeled any of the emission observed by the VLA and ALMA because the spatial resolution is not enough to resolve the lensed emission. Code `uvmcmcfit` assumes a predefined shape for the background source (elliptical Gaussian profile) and that the lens galaxy can be described by singular isothermal ellipsoid (SIE) profiles. The lensed dust emission in SDP.9 and SDP.11 observed by the SMA was already modeled in Bussmann et al. (2013) with an initial version of `uvmcmcfit` based on the use of GRAVLENS (Keeton 2001). However, for consistency, we have also modeled the SMA emission in our two sources with the last version of `uvmcmcfit`, the same as the one used to model the CO lines. The derived amplification values from dust continuum and CO emission are given in Table 1 (uncertainties are derived from the FWHM of the posterior probability distribution function), along with the amplifications derived for the stellar emission by Dye et al. (2014) based on the model of the emission observed by *HST*.

The magnification factors derived from the dust continuum SMA maps will be used to estimate the intrinsic IR luminosities. They will be also used to de-magnify the dense molecular gas emission. This is because the dense molecular gas traces the regions where star formation is taking place, so it might be expected that they are both spatially coincident (but see later a note on differential amplification). The magnification derived from the ^{12}CO(3–2) emission will be used to derive the de-magnified CO luminosities. Low-*J* CO emission might be more extended than mid- and high-*J* CO transitions in dusty high-redshift starbursts (Ivison et al. 2011; Riechers et al. 2011a), and dust emission might not be fully coincident with the dense molecular gas emission. Different spatial distributions of the different ISM components would imply differential amplification (Spilker et al. 2015). Since there is no high spatial resolution data for the low-*J* CO and any of the HCN, HCO$^+$, and HNC transitions, we need to assume that their amplification factors are similar to those derived from the ^{12}CO(3–2) line and dust continuum emission, respectively. The possible differential magnification between different transitions represents one of the main sources of uncertainty in the analysis presented in this work.

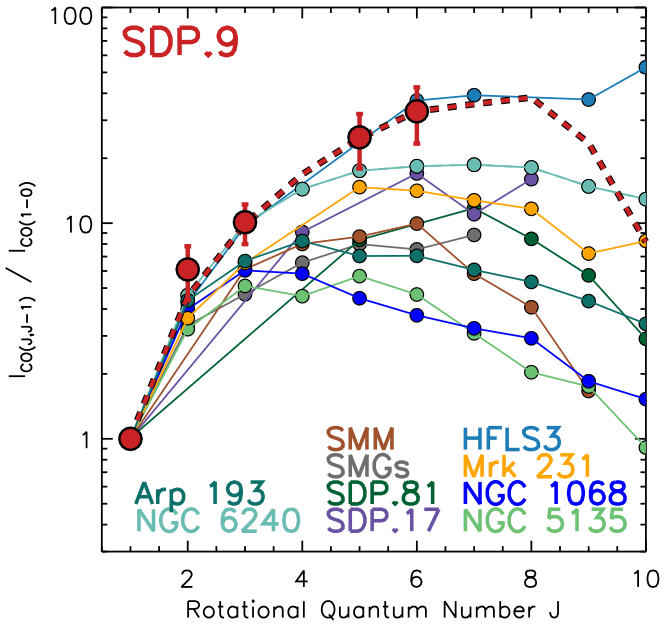

Figure 2. CO SLED of SDP.9 (red), with velocity-integrated line fluxes in units of Jy km s^{-1}. Red points are the line fluxes included in Table 1, whereas the red dashed curve is the best-fit model. We also include the CO SLED for other lensed ULIRGs at high redshift (Frayer et al. 2011; Harris et al. 2012; Iono et al. 2012; Lupu et al. 2012; Omont et al. 2013; ALMA Partnership et al. 2015), the classical population of submillimeter galaxies (Bothwell et al. 2013), the lensed SMG SMM J2135−0102 at $z \sim 2.3$ (labeled as SMM, Danielson et al. 2011), HFLS3 at $z \sim 6.34$ (Riechers et al. 2013), and several local (U) LIRGs (Meijerink et al. 2013; Papadopoulos et al. 2014; Rosenberg et al. 2015). It can be seen that SDP.9 is a highly excited source (but not as excited as local AGNs such as Mrk 231), whose CO SLED resembles the one for HFLS3.

4. Results and Discussion

4.1. Resolved Stellar, Gas, and Dust Emission

Figure 1 shows the lensed stellar emission observed with *HST* (the foreground lensing source has been subtracted using GALFIT) compared to the resolved dust (observed by SMA and PdBI), molecular gas (observed by PdBI), and radio continuum (observed by VLA) emission. Dust absorbs the rest-frame UV stellar light emitted by massive OB stars at rest-frame UV, which is, in turn, re-emitted at FIR wavelengths. Therefore, there are two main components contributing to the total SFR in star-forming galaxies, one unobscured component traced by rest-frame UV emission and one obscured component traced by FIR emission. This simplified picture is exactly what we are witnessing in Figure 1. The dust emission detected by the SMA and PdBI represents the obscured star formation, and it is preferentially located in regions where stellar light is faint, because it has been absorbed. On the other hand, stellar emission is detected in dust-poor regions, where no dust or molecular gas emission is detected.

4.2. The CO SLED

In order to analyze the excitation conditions of the molecular gas in SDP.9, we have modeled its CO SLED by using all available CO line data, taken from this and previous work (see Table 1). It should be noted that, due to lack of low-J ($J_{up} \leqslant 3$) ^{12}CO observations for SDP.11, which trace the bulk of its molecular gas, we only study in this work the CO SLED of SDP.9 (Figure 2). The inclusion of the ^{12}CO(1–0) and ^{12}CO(3–2) transitions in SDP.9 improves the sampling of the CO SLED in this source with respect to the analysis presented in Lupu et al. (2012). The ^{12}CO(3–2) emission had been already presented in Omont et al. (2013) at low spatial resolution, and with a line flux similar to the one reported here from our high spatial resolution data. For a reference, we also include in Figure 2 the CO SLED of different sources: the classical submillimeter galaxy (SMG) population (Bothwell et al. 2013), high-redshift lensed ULIRGs (Frayer et al. 2011; Harris et al. 2012; Lupu et al. 2012; ALMA Partnership et al. 2015), HFLS3 at $z \sim 6.34$ (Riechers et al. 2013), and local (U) LIRGs (Papadopoulos et al. 2014; Rosenberg et al. 2015). The shape of the observed CO SLED reveals a highly excited molecular ISM in SDP.9, much more excited than the average SMG (median redshift of $z \sim 2.3$), SDP.81 at $z \sim 3$, slightly more excited than some local merger/starbursts such as NGC 6240 (Papadopoulos et al. 2014), and less excited than some local AGNs such as Mrk 231. The similarity between the CO SLED of SDP.9 and HFLS3 is very remarkable.

In order to model the CO line ladder in SDP.9, we use the non-LTE radiative transfer code Myradex,[22] with an escape probability of $\beta = (1 - e^{-\tau})/\tau$ in an expanding spherical geometry. MyRadex solves the same problem as RADEX (van der Tak et al. 2007), but with a different approach to solve the statistical equilibrium problem. We adopt a CO abundance relative to H_2 of 10^{-4}. The CMB temperature is set to $T_{CMB} = 7.004$ K. We made a grid of CO line ladders with the following parameter ranges: number density of molecular hydrogen $n_{H_2} = 10^2$–10^8 cm^{-3}, kinetic temperature $T_{kin} = 10^{0.5}$–10^3 K, and velocity gradient $dv/dr = 1$–10^3 km s^{-1} pc^{-1}. We then convert the velocity gradient to column density, where the latter is used as an input for Myradex, following Zhang et al. (2014b). From the model grid, we calculate the likelihood distributions for all parameter combinations following Ward et al. (2003). We assume that the CO column length is less than 2 times the CO-emitting size. We marginalize the parameters by integrating the likelihood distribution over all other parameters. The best fit gives the following results: $n(H_2) = 3.2 \times 10^5$ cm^{-3}, $dv/dr = 18.2$ km s^{-1} pc^{-1}, $T_{kin} = 10^{1.7}$ K, $N_{H_2} = 2.5 \times 10^{22}$, $M_{H_2} = 1.3 \times 10^{11}\,M_\odot$, and $X_{CO} = 1.0$ K km s^{-1} cm^{-2}. Therefore, the modeling of its CO SLED suggests that the molecular gas in SDP.9 is likely dominated by a warm and dense component, which is much more excited than the average submillimeter population at higher redshift (Bothwell et al. 2013).

4.3. Dense Molecular Gas Tracers in High-redshift Starbursts

Figures 3 and 4 show the HCN(3–2), HCO$^+$(3–2), and HNC (3–2) spectra of SDP.9 and SDP.11, respectively, along with previously detected lines in these sources. Thanks to the depth provided by the ALMA and VLA observations, all dense $J = 3$–2 transitions and HCN(1–0) and HCO$^+$(1–0) lines have been detected in SDP.9. In SDP.11, the HCN(3–2) and HCO$^+$(3–2) transitions have been detected. The velocity-integrated line fluxes (and 3σ upper limits) of all observed transitions are shown in Table 1. All velocity-integrated line fluxes have been calculated from the zero-moment maps. To calculate the upper limit for the nondetected transitions, we have assumed that their width is the same as the mid-J CO lines and that there is no velocity offset with respect to the detected dense gas tracers.

[22] https://github.com/fjdu/myRadex

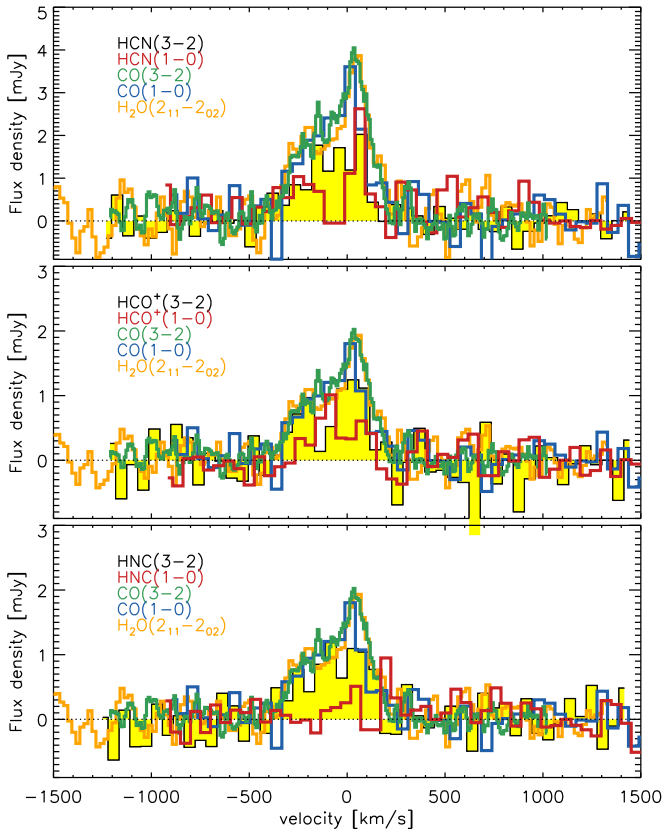

Figure 3. ALMA spectra of the detected HCN, HCO^+, and HNC lines in SDP.9. We also show the available CO(3–2) (PdBI; this work), CO(1–0) (VLA; this work), and $H_2O(2_{11}–2_{02})$ (from Omont et al. 2013) transitions in the three panels. The CO and water lines are replicated on each panel to compare their profiles with the dense molecular gas tracer line profiles. The *y*-axes of all panels indicate the flux density of the HCN, HCO^+, and HNC emission lines. The other transitions have been rescaled for the sake of clarity. It should be noted that the HCN(1–0) and HCO^+(1–0) spectra are not shown here since the line emission is only detected after collapsing the data cube over the same velocity range where the CO and water lines are detected. It can be seen that the CO and water line profiles are very similar for this source (indicating that the CO gas and H_2O gas are spatially coincident as reported in Omont et al. 2013 and Yang et al. 2016), but slightly different from the dense molecular gas transitions.

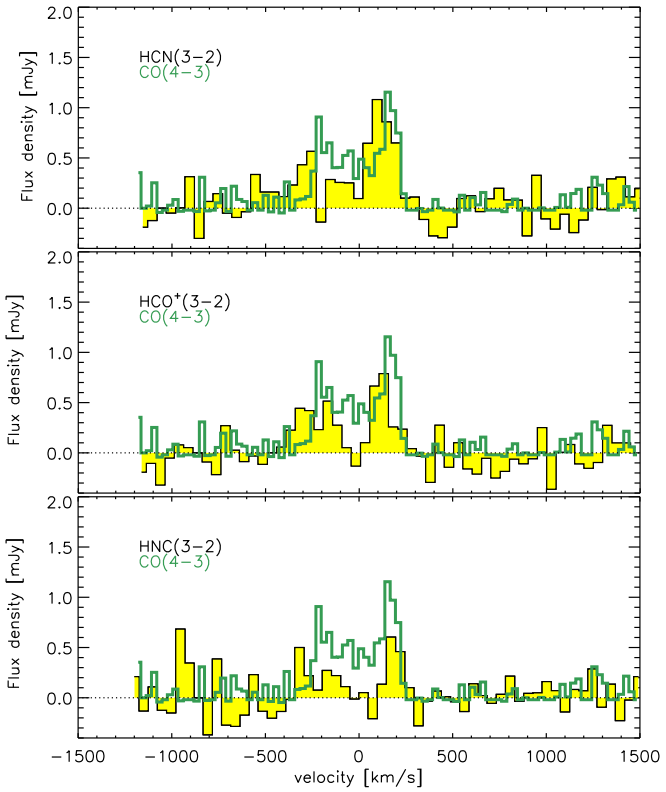

Figure 4. Similar to Figure 3, but for SDP.11. We do not show here the $J = 1$–0 transitions of the dense molecular gas tracers because none of them have been detected for this source.

In SDP.9, the widths of the HCN(3–2), HCO^+(3–2), and HNC(3–2) transitions are similar to the CO and water lines and are also centered at the same velocity. However, it seems (although the relatively low S/N prevents robust results) that the line profiles are slightly different. In contrast, despite that the molecular gas lines in SDP.11 have similar profiles, they are shifted with respect to each other by $\sim$100 km s^{-1}, with the shift being more evident in the HCN(3–2). The different line profiles and velocity offsets (taken with caution, as the S/N of the line profiles is not superb) might suggest that the different transitions are arising from different places across the galaxies. These results add to the similarities and differences found between dense and CO lines in previous analysis of high-redshift sources. For example, Riechers et al. (2011b) found that the HCO^+(4–3) transition in the Cloverleaf quasar at $z = 2.56$ is narrower than the CO lines, suggesting that the densest gas is more spatially concentrated. Furthermore, Danielson et al. (2011) found that the velocity centroid of the HCN(3–2) emission in SMM J2135-0102, a lensed SMG at $z \sim 2.3$, is redshifted by approximately $\sim$230 $\pm$ 100 km s^{-1} with respect to the redshift derived from ^{12}CO lines.

4.4. The HCN and HCO^+ SLED

Figure 5 shows the 3–2 to 1–0 luminosity ratio for the HCN and HCO^+ transitions in SDP.9 and SDP.11 (note that only upper limits are available for SDP.11 because the $J = 1$–0 transitions have not been detected for this source). We see that the HCN(3–2)/HCN(1–0) line ratio in both sources is in agreement with the highest values found in local galaxies. The HCN(3–2)/HCN(1–0) line ratios could actually be compatible with a trend suggesting higher excitation in more IR-luminous galaxies. On the other hand, the HCO^+(3–2)/HCO^+(1–0) line ratios of SDP.9 and SDP.11 are similar to the average value found in local starbursts (Graciá-Carpio et al. 2008; Juneau et al. 2009), which does not seem to correlate with the total IR luminosity, although no HCO^+ transitions have been detected at the low-luminosity end. The line HCN SLED of SDP.9 is also compatible with that found for Arp 193, a classical starburst in the local universe, but suggests a less excited dense molecular gas reservoir than in NGC 6240 (Papadopoulos et al. 2014). All these results suggest that the excitation conditions of the dense molecular gas in some high-redshift sources are not significantly different from what can be found in the local universe, despite that SDP.9 and SDP.11 are more luminous than most low-redshift sources studied so far in HCN and HCO^+.

We have also fitted the CO and HCN SLEDs of SDP.9 simultaneously with the single excitation component large velocity gradient (LVG) modeling. To do this, we have assumed that both CO and HCN transitions come from the same region with the same excitation conditions. We keep the HCN abundance (relative to H_2) to be 2×10^{-8}, which is an average value in local galaxies (Omont 2007; Krips

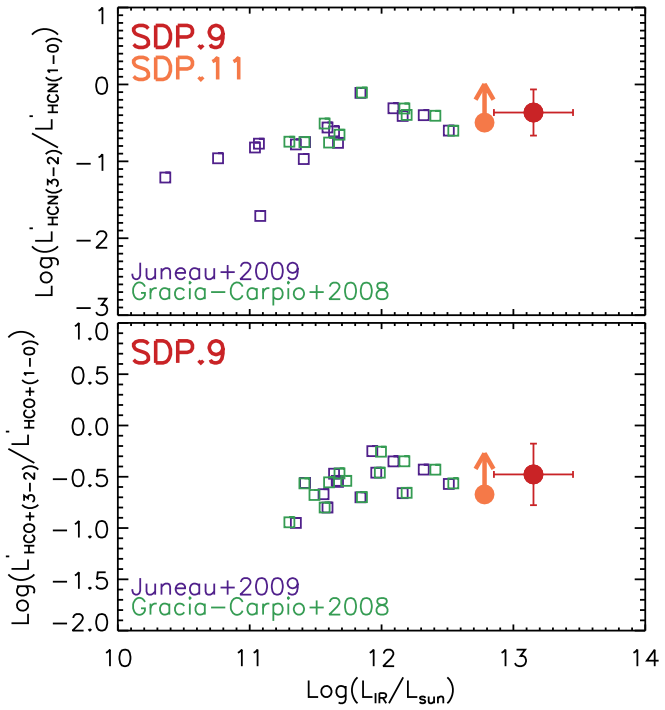

Figure 5. Ratio between the 3–2 and 1–0 transitions of the dense molecular gas tracers HCN (top panel) and HCO^+ (bottom panel) in SDP.9 and SDP.11 (for the latter only upper limits are available because the $J = 1$–0 transitions have not been detected at the depth of our VLA observations). These are compared with the values found for local star-forming galaxies (Graciá-Carpio et al. 2008; Juneau et al. 2009). We see that the line ratios in both sources are compatible with those found for local sources at comparable luminosities (actually meaning slightly lower since our sources are among the brightest studied so far in HCN and HCO^+), suggesting similar excitation conditions.

et al. 2008). We derive the likelihood distributions for both grids of HCN and CO and marginalize the matrix in the same way as in Section 4.2. The best fit gives the following results: $n(H_2) = 10^{4.5}$ cm^{-3}, $T_{\rm kin} = 10^{1.8}$ K, $dv/dr = 10^{1.48}$ km s^{-1} pc^{-1}, $N(H_2) = 10^{22.5}$, $M(H_2) = 10^{11.2}\,M_\odot$, and $X_{\rm CO} = 1.4$ K km s^{-1} cm^{-2}. We see that the $T_{\rm kin}$ and column density are consistent with the CO-based results. However, the H_2 volume density is $\rho = 10^{4.5}$ cm^{-3}, lower than the CO-based value. It is likely because the CO excitation is close to an LTE condition that it is not sensitive to density.

4.5. The L_{IR}–L'_{dense} Relations at High Redshift

Figure 6 compares the total IR and dense molecular gas luminosities of SDP.9 and SDP.11 with a sample of local and high-redshift starbursts and QSOs taken from the literature (Greve et al. 2006; Riechers et al. 2006; Gao et al. 2007; Bussmann et al. 2008; Graciá-Carpio et al. 2008; Juneau et al. 2009; Danielson et al. 2011; García-Burillo et al. 2012). It should be pointed out that the line fluxes reported in Bussmann et al. (2008) and Juneau et al. (2009) do not seem to take into account the fact that their galaxies are larger than the beam size of their single-dish observations, thus missing a fraction of the dense gas line fluxes. We see that the correlation between IR and line luminosity for both low-redshift galaxies and SDP.9 and SDP.11 can be described by a single relation. Therefore, we find no clear evidence of enhanced SFR at a given line luminosity in SDP.9 and SDP.11 when compared to local LIRGs/ULIRGs. This is mainly because the correlation between $L_{\rm IR}$ and $L_{\rm dense}$ for local galaxies is not especially tight, but instead has a significant dispersion of ± 0.5 dex (see Figure 6).

The detected HCN(3–2) emission in SMM J2135-0102 reported by Danielson et al. (2011) has line and IR luminosities that are also in agreement with the spread of the local correlation, also supporting the fact that a single relation can be applied at low and high redshift (Greve et al. 2006). Gao et al. (2007) presented HCN(1–0) observations of two SMGs and two QSOs and compiled previous HCN(1–0) detections and upper limits from the literature to conclude that high-redshift sources systematically lie above FIR/HCN correlation for nearby galaxies by about a factor of 2. This does not seem to be in agreement with our results for SDP.9 and SDP.11. However, it should be pointed out that the sample used in Gao et al. (2007) has a significant contribution of high-redshift QSOs (even at redshift $z \sim 6$) whose dense molecular gas properties do not necessarily have to be similar to the classical population of high-redshift SMGs (median redshift of $z \sim 2.3$; Chapman et al. 2005) or $z \sim 1$ ULIRGs as studied here. Furthermore, the total IR luminosities in the former sources might be affected by the AGNs, so not all of the total IR luminosity is due to star formation. If that was actually the case, and only the total IR luminosity due to star formation was considered, the points would be closer to the local relation. Riechers et al. (2006) reported detections of HCN(1–0) and HCO^+(1–0) in the Cloverleaf quasar at $z = 2.56$, and their points are also compatible with the local relation (see Figure 7).

The fact that, as suggested by our results, the same relation between total IR and dense gas luminosities can be applied to galaxies at both low and high redshift might indicate that some high-redshift sources are more IR luminous (have higher SFR) just because they have more dense molecular gas.

It has been obtained in various previous works that the relation between $L_{\rm IR}$ and $L'_{\rm HCN}$ from $J \geqslant 1$ has a slope equal to 1, meaning that all those dense gas tracers are correlated with the SFR, and indicating that the SFR in the dense gas is not likely affected by the free-fall time (Zhang et al. 2014a). Actually, because the free-fall time is related to the density by $\tau_{\rm ff} \propto n^{-0.5}$, it would be lower for higher-J transitions, but still a similar $L_{\rm IR}$–$L_{\rm dense}$ relation is seen for ^{12}CO(1–0), ^{12}CO(4–3), HCN(1–0), HCN(4–3), and other dense gas tracers (Wu et al. 2010; Reiter et al. 2011; Greve et al. 2014; Zhang et al. 2014a). We have represented a fit with slope equal to unity with the black dashed lines in Figure 6. It can be seen that, for the HCN(1–0) transition, and within the uncertainties, SDP.9 is still compatible with a linear relation, and actually most previous fits to the $L_{\rm IR}$–$L_{\rm HCN(1-0)}$ are compatible with a linear relation (García-Burillo et al. 2012; Privon et al. 2015). The same seems to be true for the HCN(3–2) transition for both SDP.9 and SDP.11, although the spread of the points for local galaxies prevents a robust determination of the slope.

4.6. The Dense Gas Depletion Time

The dense molecular line luminosities can be combined with the total IR luminosity of SDP.9 to determine its star formation efficiency and dense gas depletion time. We note that we do this calculation only for SDP.9 because we have not detected the dense $J = 1$–0 transitions in SDP.11. The dense-to-total IR luminosity ratio (a proxy of the star formation efficiency of the dense gas phase) in SDP.9 is $L'_{\rm HCN(1-0)}/L_{\rm IR} \sim 0.7 \times 10^{-3}\,L'/L_\odot$ (implying a dense gas depletion time of $\tau_{\rm dep} \sim 40$ Myr, assuming $M_{\rm dense}[M_\odot] = 10\,L'_{\rm HCN(1-0)}$ [K km s^{-1} pc^2]; see García-Burillo

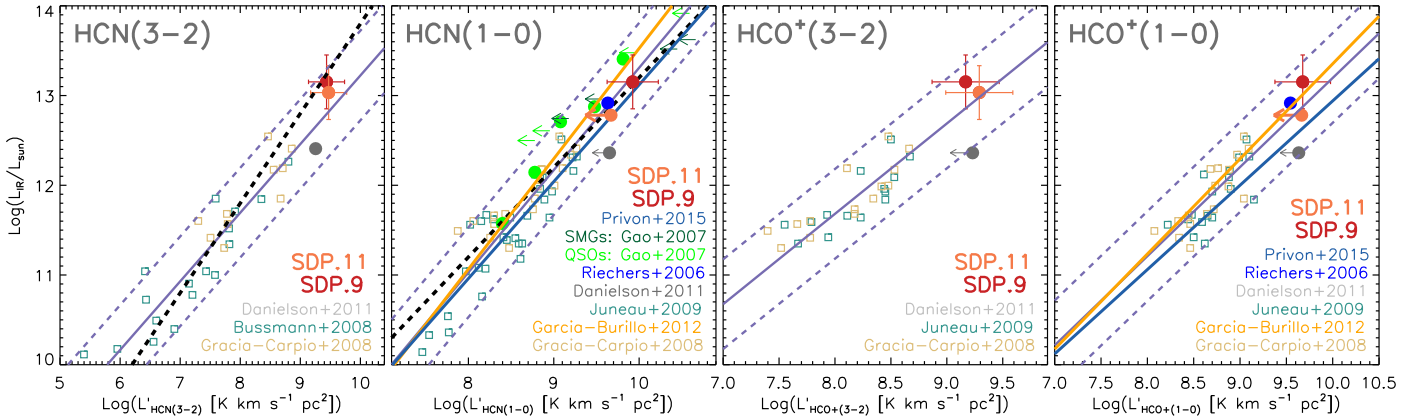

Figure 6. Relation between the total IR luminosity, $L_{\rm IR}$, and the dense molecular gas luminosities studied in this work for SDP.9 (red circles) and SDP.11 (orange circles and orange arrows for upper limits). We compare the values found for SDP.9 and SDP.11 with those obtained for different samples of local galaxies (Bussmann et al. 2008; Graciá-Carpio et al. 2008; Juneau et al. 2009) and high-redshift QSOs and SMGs from Gao et al. (2007), Riechers et al. (2006), and Danielson et al. (2011). We caution that Bussmann et al. (2008) and Juneau et al. (2009) might not have corrected their measurements for the effect that the beam of their observations did not cover the whole extension of their sources. Purple solid lines represent linear fits to all points in each panel, and purple dashed lines represent ±0.5 dex deviations from the linear fits. We also represent the correlation between $L_{\rm IR}$ and $L_{\rm HCN}$ and $L_{\rm HCO^+}$ derived in García-Burillo et al. (2012) with solid orange lines. For a reference, we include with a black dashed line a relation between $L_{\rm IR}$ and $L'_{\rm HCN(1-0)}$ with a slope equal to 1, expected for ULIRGs; see discussion in Riechers et al. (2007). However, with a relatively large scatter, all points for local and high-redshift starbursts can be fitted with a single linear relation. Therefore, the strong SFR in our galaxies is accompanied by a more massive dense molecular gas reservoir in the same proportion as in the local universe.

et al. 2012) is compatible (within the scatter) with the average value reported for LIRGs in the local universe (García-Burillo et al. 2012; Privon et al. 2015), where no significant correlation has been found between the dense gas depletion time and the total IR luminosity (Gao & Solomon 2004a). Actually, a large scatter of $L'_{\rm HCN(1-0)}/L_{\rm IR}$ values has been found in the literature, interpreted by Privon et al. (2015) as a lack of a simple link between $L'_{\rm HCN(1-0)}$ and the mass of the dense gas directly associated with star formation.

4.7. HCN, HCO^+, and HNC Line Ratios at High Redshift

4.7.1. The HCN/HNC Ratio

The top panel of Figure 7 compares the HCN(1–0)/HNC (1–0) and HCN(3–2)/HNC(3–2) line ratios in SDP.9 and SDP.11 with those for a sample of local sources from Aalto et al. (2002), Baan et al. (2008), and Costagliola et al. (2011). It has been suggested that sources can be divided into photon-dominated regions (PDRs) or X-ray dominated regions (XDRs) depending on the value of the HCN(1–0)/HNC(1–0) ratio (Meijerink et al. 2007; Baan et al. 2008; Loenen et al. 2008). XDRs (along with pumping of the rotational levels through the mid-infrared continuum) is actually one of the plausible explanations for overluminous HNC(1–0) emission in galaxies with warm molecular gas (Aalto et al. 2007). According to the models of Meijerink et al. (2007), the high HCN(1–0)/HNC (1–0) ratios found for SDP.9 and SDP.11 could be only explained by PDR-dominated regions (see also Loenen et al. 2008). This is similar to the dense gas properties of local ULIRGs (Costagliola et al. 2011), which show an average HCN(1–0)/HNC(1–0) ratio of ∼2. Actually, as shown in Figure 7, the HCN(1–0)/HNC(1–0) ratios of most local (U) LIRGs are similar to that found for SDP.9. On the other hand, the HCN(3–2)/HNC(3–2) ratios (or upper limit) found for SDP.9 and SDP.11 could be explained by either XDR or PDR models, since the HCN/HNC ratio for mid-J transitions can also be enhanced in XDRs (Meijerink et al. 2007).

As shown in Loenen et al. (2008), the high HCN(1–0)/HNC (1–0) ratios found for local galaxies, as well as for SDP.9, cannot be explained only with models in which PDR or XDR dominates (see also Costagliola et al. 2011). Instead, they show that the effect of mechanical heating (which can be produced by dissipating supernova shocks) needs to be considered (see also Kazandjian et al. 2012; Izumi et al. 2016). Loenen et al. (2008) proposed that the PDR sources can be divided into two groups: one small group that can be modeled with classical PDR chemistry and whose HCN/HNC ratios are around unity (which is not the case of SDP.9), and a second group (larger than the other one) with lower densities that are heated by mechanical heating. SDP.9 would fall into the second group owing to its high HCN(1–0)/HNC(1–0) ratio; therefore, mechanical heating should also be included as a possible source of enhanced HCN emission with respect to HNC.

4.7.2. The HCN/HCO^+ Ratio

The second panel of Figure 7 shows the HCN(1–0)/HCO^+(1–0) and HCN(3–2)/HCO^+(3–2) line ratios for SDP.9 and SDP.11 in comparison with the values for a sample of local (U)LIRGs from Graciá-Carpio et al. (2008), Baan et al. (2008), Costagliola et al. (2011), and García-Burillo et al. (2012). It can be seen that, for both $J = 1$–0 and $J = 3$–2 transitions, the HCN emission is brighter than HCO^+ in SDP.9 and SDP.11, and that the line ratios are compatible to the values found for luminous starbursts in the local universe (although not as luminous as SDP.9 or SDP.11). This might indicate that the dense molecular gas can have similar properties at high and low redshift, at least for a subsample of high-redshift galaxies.

It has been proposed in the literature that the HCN/HCO^+ ratio can be used as a tool to distinguish between AGNs and starbursts dominated by star formation. Kohno et al. (2001) suggested that the enhanced HCN in some Seyfert galaxies (with HCN/$HCO^+ > 2$, thus higher than the values found for SDP.9 and SDP.11) could originate from X-ray-irradiated dense obscuring tori, as happens in NGC 1068, NGC 1097, and NGC 5194. The higher HCN/HCO^+ ratios in AGNs have been attributed to an enhancement of the HCN line in the XDR surrounding the AGN (Lepp & Dalgarno 1996). However,

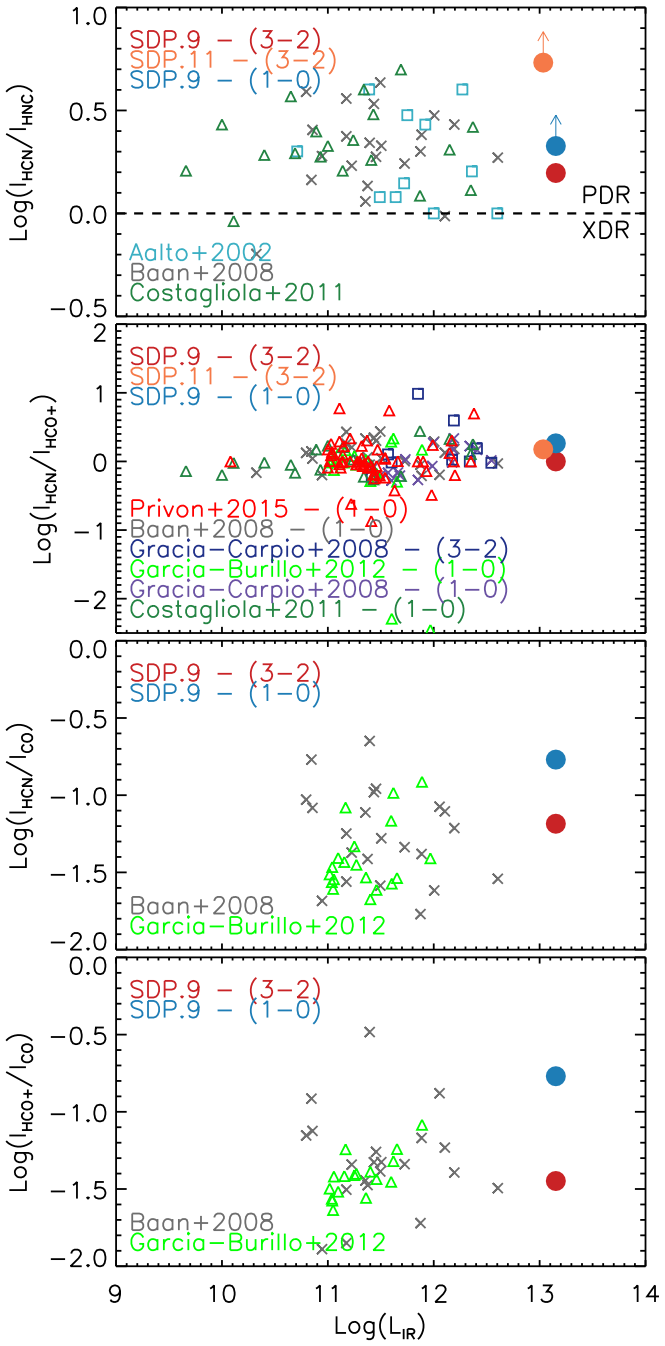

Figure 7. Line flux ratios for SDP.9 and SDP.11 compared with trends found in local sources. Each panel corresponds to a different line ratio, as indicated by each legend. Note that the similarity in the HCN/HCO$^+$ for SDP.9 makes the red circle appear behind the blue one.

Costagliola et al. (2011) claimed that the HCN/HCO$^+$ ratio is not a reliable tracer of XDRs. Furthermore, Privon et al. (2015) recently showed that the HCN/HCO$^+$ ratio in galaxies dominated by star formation can be as high as those found in AGNs. Actually, Privon et al. (2015) showed that neither the hardness of the X-ray spectrum nor the total X-ray luminosity correlates with the HCN/HCO$^+$ ratio, suggesting that XDRs are not always the major driver in enhancing the HCN(1–0) emission in luminous starbursts, possibly because the XDRs are spatially disconnected from the regions that dominate the global line luminosity.

The HCN emission in molecular clouds can also be enhanced by mid-IR pumping of a 14 μm vibrational band (Aalto et al. 1995). Additionally, it has also been claimed that the HCN/HCO$^+$ ratio can also be enhanced in compact environments, since in this case self-absorption is more likely to happen in HCO+ than in HCN (Aalto et al. 2015). On the other hand, the HCO$^+$ emission can be enhanced (so decreasing the HCN/HCO$^+$ ratio) by mid-IR pumping via the 12 μm vibrational band (Graciá-Carpio et al. 2006), and its abundance is affected by cosmic rays and the ratio of cosmic ionization rate and gas density (Riechers et al. 2006). Both HCN and HCO$^+$ are sensitive to the cosmic-ray-produced abundance of H_3^+, but HCO$^+$ is an ion and therefore also very sensitive to the ambient free electron abundance. Even a small increase of the free electron fraction can lead to a severe HCO$^+$ depletion. Therefore, strong cosmic-ray ionizing radiation increases the number of H_3^+ to form HCO$^+$, but it also increases the presence of free electrons that destroy HCO$^+$ while HCN remains (see discussion in Papadopoulos 2007).

From all previous work we conclude that the number of processes affecting the observed HCN/HCO$^+$ line ratio is quite significant. Furthermore, it seems that there is no consensus about the reliability of using the HCN/HCO$^+$ line ratio as a tracer of the presence of XDRs; therefore, we do not attempt to draw any conclusion on the nature of SDP.9 and SDP.11 from this line ratio. However, it is very remarkable that the HCN/HCO$^+$ ratios for both SDP.9 and SDP.11 are similar to the values found in local (U)LIRGs. This might indicate that, whatever the processes governing that line ratio, they can be present and affecting that line ratio at both low and high redshift.

4.8. Comparing High- and Low-density Molecular Gas Tracers

The ratio between the HCN and CO low-J transitions is arguably the cleanest indicator of the the fraction of the total gas reservoir residing in the dense phase, and it has been proposed to be a unique tool to explore the star formation mode of star-forming galaxies: isolated disk versus merger-driven starbursts (Papadopoulos & Geach 2012). Figure 7 includes a comparison between the high-density (HCN and HCO$^+$ emission) and low-density (CO emission) molecular gas tracers for SDP.9, the only one of the two sources studied in this work with detections in all those transitions at both $J = 3$–2 and $J = 1$–0. While the ratio for the $J = 3$–2 transitions (both HCN/CO and HCO$^+$/CO) and the $J = 1$–0 HCO$^+$/CO are in very good agreement with the values found for local galaxies (Baan et al. 2008), the $J = 1$–0 HCN/CO ratio in SDP.9 is higher than most of the local sources. This indicates that SDP.9 contains a larger dense molecular gas reservoir with respect to the total molecular gas than those found in local galaxies. Since SDP.9 is more IR luminous than most galaxies studied so far in the local universe, their higher dense gas fraction might be associated with its higher SFR.

Assuming the relation between the dense molecular gas mass and the HCN(1–0) luminosity $M_{\rm dense} \sim 10 \times L'_{\rm HCN(1-0)}$ [K km s^{-1} pc^{-2}] (Gao & Solomon 2004b; García-Burillo et al. 2012), we obtain $M_{\rm dense} \sim 8.4 \times 10^{10}\,M_\odot$, which is slightly smaller than the total molecular gas mass estimated from the LVG modeling of the CO SLED ($M_{\rm H_2} \sim 1.3 \times 10^{11}\,M_\odot$; see Section 4.2). This suggests that a very large fraction of the molecular gas in SDP.9 is in the form of dense gas. The $L'_{\rm HCN(1-0)}/L'_{\rm CO(1-0)} \sim 0.37$ found for SDP.9

is similar to the values found for the most luminous sources in the local universe (Gao & Solomon 2004a; García-Burillo et al. 2012), and it is also compatible with a correlation indicating that more luminous galaxies have higher dense gas fractions (or equivalently higher $L'_{\rm HCN(1-0)}/L'_{\rm CO(1-0)}$ ratios).

We should point out that there are several uncertainties in the derivation of the dense molecular gas mass. As discussed in Papadopoulos et al. (2014), the $\alpha_{\rm HCN}$ factor might be lower than typically assumed in extreme starbursts if their dense gas is much warmer and/or in unbound states. Additionally, the HCN/CO line ratio traces the dense gas mass fractions only if both lines are collisionally excited. In strong starbursts, HCN can also be excited by mid-IR pumping (see also Section 4.7.2), thus producing enhanced HCN/CO line ratios without large amounts of dense molecular gas. Furthermore, the possible presence of an AGN in SDP.9 might also produce enhanced HCN luminosity (Privon et al. 2015).

As mentioned above, observations of local galaxies conclude that the $J = 1$–0 HCN/CO line ratio is an excellent way to discriminate between different star formation modes. Compact, merger-driven, extreme starbursts are associated with high $J = 1$–0 HCN/CO ratios, whereas lower values are found for isolated star-forming disks with more extended star formation (Solomon et al. 1992; Gao & Solomon 2004b). SDP.9 might belong to the former group as expected from its high IR luminosity (Engel et al. 2010), and, in fact, the $L'_{\rm HCN}/L'_{\rm CO}$ luminosity ratio of SDP.9 is compatible with it being a merger-driven starburst.

According to the models presented in Meijerink et al. (2007), the HCN/CO ratio in SDP.9 suggests a density of $\sim$(2–3) $\times$ 10^5 cm^{-3}, which is compatible with the density derived from the LVG modeling of the CO SLED, $n_{\rm H_2} \sim 3.2 \times 10^5$ cm^{-3} (see Section 4.2).

5. Conclusions

In this work we have presented ALMA and VLA observations of dense molecular gas tracers in two lensed ULIRGs at $z \sim 1.6$ selected from the *H*-ATLAS survey. The main conclusions of our work are as follows:

1. We have detected HCN(3–2), HCO$^+$(3–2), HNC(3–2), HCN(1–0), and HCO$^+$(1–0) in SDP.9, as well as HCN (3–2) and HCO$^+$(3–2) in SDP.11. This clearly highlights the power of ALMA and VLA to carry out studies of the dense molecular gas in high-redshift dusty starbursts.
2. The CO SLED of SDP.9 indicates that its molecular gas is likely dominated by one warm and dense component. The molecular gas traced by CO emission in SDP.9 is more excited than the average SMG and other lensed IR-bright sources at $z \sim 2.5$ and compatible with the excitation found in some local AGNs.
3. The total IR and dense molecular line luminosities of both SDP.9 and SDP.11 are compatible with the $L_{\rm IR}$–$L_{\rm dense}$ relations found for star-forming galaxies in the local universe. This might indicate that the higher SFR in high-redshift dusty starbursts is driven by a higher dense molecular gas mass fraction. Actually, the $L'_{\rm HCN(1-0)}/L'_{\rm CO(1-0)}$ ratio (which is significantly higher than the average ratio found for (U)LIRGs in the local universe) suggests that a large fraction of the molecular gas in SDP.9 is in the form of dense gas.
4. The HCN/HNC ratios in SDP.9 and SDP.11 suggest that these galaxies are dominated by photon-dominated regions, similar to what happens to most (U)LIRGs in the local universe. Similarly, the HCN/HCO$^+$ ratios in both sources are similar to those found for local (U) LIRGs, suggesting that the dense molecular ISM in local and some high-redshift starbursts might be very similar.

I.O., R.J.I., Z.-Y.Z., and L.D. acknowledge support from the European Research Council in the form of the Advanced Investigator Programme, 321302, COSMICISM. D.R. acknowledges support from the National Science Foundation under grant No. AST-1614213 to Cornell University. H.D. acknowledges financial support from the Spanish Ministry of Economy and Competitiveness (MINECO) under the 2014 Ramón y Cajal program MINECO RYC-2014-15686. I.O. acknowledges the warm welcome of Institute of Astrophysics of Paris (IAP), where a significant part of the analysis presented in this paper was carried out. I.O. also acknowledges the PNCG (Programme National Cosmologie Galaxies) for support in his stay at IAP. I.O. also acknowledges fruitful conversations with Padelis P. Papadopoulos and George Privon. C.F. acknowledges funding from CAPES (proc. 12203-1). M.N. acknowledges financial support from the European Union's Horizon 2020 research and innovation programme under the Marie Skłodowska-Curie grant agreement No. 707601. This work is based on observations carried out with the VLA. The NRAO is a facility of the NSF operated under cooperative agreement by Associated Universities, Inc. Based on observations carried out with the IRAM PdBI Interferometer. IRAM is supported by INSU/CNRS (France), MPG (Germany), and IGN (Spain). This paper makes use of the following ALMA data: ADS/JAO.ALMA#2012.1.00915.S. ALMA is a partnership of ESO (representing its member states), NSF (USA), and NINS (Japan), together with NRC (Canada), NSC and ASIAA (Taiwan), and KASI (Republic of Korea), in cooperation with the Republic of Chile. The Joint ALMA Observatory is operated by ESO, AUI/NRAO, and NAOJ.

Herschel is an ESA space observatory with science instruments provided by European-led Principal Investigator consortia and with important participation from NASA. The *Herschel* spacecraft was designed, built, tested, and launched under a contract to ESA managed by the *Herschel*/*Planck* Project team by an industrial consortium under the overall responsibility of the prime contractor Thales Alenia Space (Cannes), and including Astrium (Friedrichshafen) responsible for the payload module and for system testing at spacecraft level, Thales Alenia Space (Turin) responsible for the service module, and Astrium (Toulouse) responsible for the telescope, with in excess of 100 subcontractors. The *Herschel*-ATLAS is a project with *Herschel*. The *H*-ATLAS website is http://www.h-atlas.org/. U.S. participants in *H*-ATLAS acknowledge support from NASA through a contract from JPL. SPIRE has been developed by a consortium of institutes led by Cardiff University (UK) and including University of Lethbridge (Canada); NAOC (China); CEA and LAM (France); IFSI and University of Padua (Italy); IAC (Spain); Stockholm Observatory (Sweden); Imperial College London, RAL, UCL-MSSL, UKATC, and University of Sussex (UK); and Caltech, JPL, NHSC, and University of Colorado (USA). This development has been supported by national funding agencies: CSA

(Canada); NAOC (China); CEA, CNES, CNRS (France); ASI (Italy); MCINN (Spain); SNSB (Sweden); STFC, UKSA (UK); and NASA (USA). The SMA is a joint project between the Smithsonian Astrophysical Observatory and the Academia Sinica Institute of Astronomy and Astrophysics and is funded by the Smithsonian Institution and the Academia Sinica. The authors wish to recognize and acknowledge the very significant cultural role and reverence that the summit of Maunakea has always had within the indigenous Hawaiian community. We are most fortunate to have the opportunity to conduct observations from this mountain.

ORCID iDs

I. Oteo https://orcid.org/0000-0001-5875-3388
C. Yang https://orcid.org/0000-0002-8117-9991
R. J. Ivison https://orcid.org/0000-0001-5118-1313
A. Omont https://orcid.org/0000-0002-4721-3922
H. Dannerbauer https://orcid.org/0000-0001-7147-3575
C. Furlanetto https://orcid.org/0000-0001-6838-431X
H. Nayyeri https://orcid.org/0000-0001-8242-9983
R. Neri https://orcid.org/0000-0002-7176-4046
D. Riechers https://orcid.org/0000-0001-9585-1462
P. Van der Werf https://orcid.org/0000-0001-5434-5942

References

Aalto, S., Booth, R. S., Black, J. H., & Johansson, L. E. B. 1995, A&A, 300, 369
Aalto, S., Polatidis, A. G., Hüttemeister, S., & Curran, S. J. 2002, A&A, 381, 783
Aalto, S., Spaans, M., Wiedner, M. C., & Hüttemeister, S. 2007, A&A, 464, 193
Aalto, S., Martín, S., Costagliola, F., et al. 2015, A&A, 584, A42
ALMA Partnership et al. 2015, ApJL, 808, L4
Baan, W. A., Henkel, C., Loenen, A. F., Baudry, A., & Wiklind, T. 2008, A&A, 477, 747
Bothwell, M. S., Smail, I., Chapman, S. C., et al. 2013, MNRAS, 429, 3047
Bussmann, R. S., Narayanan, D., Shirley, Y. L., et al. 2008, ApJL, 681, L73
Bussmann, R. S., Pérez-Fournon, I., Amber, S., et al. 2013, ApJ, 779, 25
Bussmann, R. S., Riechers, D., Fialkov, A., et al. 2015, ApJ, 812, 43
Chapman, S. C., Blain, A. W., Smail, I., & Ivison, R. J. 2005, ApJ, 622, 772
Chen, H., Braine, J., Gao, Y., Koda, J., & Gu, Q. 2017, ApJ, 836, 101
Costagliola, F., Aalto, S., Rodriguez, M. I., et al. 2011, A&A, 528, A30
Danielson, A. L. R., Swinbank, A. M., Smail, I., et al. 2011, MNRAS, 410, 1687
Davies, R., Mark, D., & Sternberg, A. 2012, A&A, 537, A133
Dye, S., Negrello, M., Hopwood, R., et al. 2014, MNRAS, 440, 2013
Eales, S., Dunne, L., Clements, D., et al. 2010, PASP, 122, 499
Engel, H., Tacconi, L. J., Davies, R. I., et al. 2010, ApJ, 724, 233
Frayer, D. T., Harris, A. I., Baker, A. J., et al. 2011, ApJL, 726, L22
Gao, Y., Carilli, C. L., Solomon, P. M., & Vanden Bout, P. A. 2007, ApJL, 660, L93
Gao, Y., & Solomon, P. M. 2004a, ApJ, 606, 271
Gao, Y., & Solomon, P. M. 2004b, ApJS, 152, 63
García-Burillo, S., Usero, A., Alonso-Herrero, A., et al. 2012, A&A, 539, A8
García-Burillo, S., Combes, F., Usero, A., et al. 2014, A&A, 567, A125
Graciá-Carpio, J., García-Burillo, S., Planesas, P., & Colina, L. 2006, ApJL, 640, L135
Graciá-Carpio, J., García-Burillo, S., Planesas, P., Fuente, A., & Usero, A. 2008, A&A, 479, 703
Greve, T. R., Hainline, L. J., Blain, A. W., et al. 2006, AJ, 132, 1938
Greve, T. R., Leonidaki, I., Xilouris, E. M., et al. 2014, ApJ, 794, 142
Harris, A. I., Baker, A. J., Frayer, D. T., et al. 2012, ApJ, 752, 152
Imanishi, M., Nakanishi, K., Tamura, Y., Oi, N., & Kohno, K. 2007, AJ, 134, 2366
Imanishi, M., Nakanishi, K., Tamura, Y., & Peng, C.-H. 2009, AJ, 137, 3581
Iono, D., Hatsukade, B., Kohno, K., et al. 2012, PASJ, 64, 2
Ivison, R. J., Papadopoulos, P. P., Smail, I., et al. 2011, MNRAS, 412, 1913
Izumi, T., Kohno, K., Aalto, S., et al. 2016, ApJ, 818, 42
Juneau, S., Narayanan, D. T., Moustakas, J., et al. 2009, ApJ, 707, 1217
Kauffmann, J., Pillai, T., & Zhang, Q. 2013, ApJL, 765, L35
Kazandjian, M. V., Meijerink, R., Pelupessy, I., Israel, F. P., & Spaans, M. 2012, A&A, 542, A65
Keeton, C. R. 2001, arXiv:astro-ph/0102340
Kohno, K., Matsushita, S., Vila-Vilaró, B., et al. 2001, in ASP Conf. Ser. 249, The Central Kiloparsec of Starbursts and AGN: The La Palma Connection, ed. J. H. Knapen et al. (San Francisco, CA: ASP), 672
Krips, M., Neri, R., García-Burillo, S., et al. 2008, ApJ, 677, 262
Lepp, S., & Dalgarno, A. 1996, A&A, 306, L21
Liu, L., Gao, Y., & Greve, T. R. 2015, ApJ, 805, 31
Loenen, A. F., Spaans, M., Baan, W. A., & Meijerink, R. 2008, A&A, 488, L5
Longmore, S. N., et al. 2013, MNRAS, 429, 987
Lupu, R. E., Scott, K. S., Aguirre, J. E., et al. 2012, ApJ, 757, 135
Meijerink, R., Spaans, M., & Israel, F. P. 2007, A&A, 461, 793
Meijerink, R., Kristensen, L. E., Weiß, A., et al. 2013, ApJL, 762, L16
Negrello, M., Hopwood, R., De Zotti, G., et al. 2010, Sci, 330, 800
Negrello, M., Hopwood, R., Dye, S., et al. 2014, MNRAS, 440, 1999
Omont, A. 2007, RPPh, 70, 1099
Omont, A., Yang, C., Cox, P., et al. 2013, A&A, 551, A115
Papadopoulos, P. P. 2007, ApJ, 656, 792
Papadopoulos, P. P., & Geach, J. E. 2012, ApJ, 757, 157
Papadopoulos, P. P., Zhang, Z.-Y., Xilouris, E. M., et al. 2014, ApJ, 788, 153
Privon, G. C., Herrero-Illana, R., Evans, A. S., et al. 2015, ApJ, 814, 39
Reiter, M., Shirley, Y. L., Wu, J., et al. 2011, ApJS, 195, 1
Riechers, D. A., Hodge, J., Walter, F., Carilli, C. L., & Bertoldi, F. 2011a, ApJL, 739, L31
Riechers, D. A., Walter, F., Carilli, C. L., et al. 2006, ApJL, 645, L13
Riechers, D. A., Walter, F., Carilli, C. L., et al. 2011b, ApJ, 726, 50
Riechers, D. A., Walter, F., Carilli, C. L., & Bertoldi, F. 2007, ApJL, 671, L13
Riechers, D. A., Bradford, C. M., Clements, D. L., et al. 2013, Natur, 496, 329
Rosenberg, M. J. F., van der Werf, P. P., Aalto, S., et al. 2015, ApJ, 801, 72
Shirley, Y. L. 2015, PASP, 127, 299
Solomon, P. M., Downes, D., & Radford, S. J. E. 1992, ApJL, 387, L55
Spilker, J. S., Aravena, M., Marrone, D. P., et al. 2015, ApJ, 811, 124
Ueda, J., Iono, D., Petitpas, G., et al. 2012, ApJ, 745, 65
van der Tak, F. F. S., Black, J. H., Schöier, F. L., Jansen, D. J., & van Dishoeck, E. F. 2007, A&A, 468, 627
Ward, J. S., Zmuidzinas, J., Harris, A. I., & Isaak, K. G. 2003, ApJ, 587, 171
Wu, J., Evans, N. J., II, Shirley, Y. L., & Knez, C. 2010, ApJS, 188, 313
Yang, C., Omont, A., Beelen, A., et al. 2016, A&A, 595, A80
Zhang, Z.-Y., Gao, Y., Henkel, C., et al. 2014a, ApJL, 784, L31
Zhang, Z.-Y., Henkel, C., Gao, Y., et al. 2014b, A&A, 568, A122